Quantitative Localized Proton-Promoted Dissolution Kinetics of Calcite using Scanning Electrochemical Microscopy (SECM)

Carrie-Anne McGeouch,[1] Massimo Peruffo,[1] Martin A. Edwards,[1,2] Lucy A. Bindley,[1] Robert A. Lazenby,[1] Michael M. Mbogoro[1], Kim McKelvey[1,2] and Patrick R. Unwin[1*]

[1] Electrochemistry and Interfaces Group, Department of Chemistry, University of Warwick, Coventry, CV4 7AL, UK.

[2] Molecular Organization and Assembly in Cells, Doctoral Training Centre, University of Warwick, Coventry, CV4 7AL, UK.

* p.r.unwin@warwick.ac.uk

Abstract

Scanning electrochemical microscopy (SECM) has been used to determine quantitatively the kinetics of proton-promoted dissolution of the calcite $(10\bar{1}4)$ cleavage surface (from natural 'Iceland Spar') at the microscopic scale. By working under conditions where the probe size is much less than the characteristic dislocation spacing (as revealed from etching), it has been possible to measure kinetics mainly in regions of the surface which are free from dislocations, for the first time. To clearly reveal the locations of measurements, studies focused on cleaved 'mirror' surfaces, where one of the two faces produced by cleavage was etched freely to reveal defects intersecting the surface, while the other (mirror) face was etched locally (and quantitatively) using SECM to generate high proton fluxes with a 25 μm diameter Pt disk ultramicroelectrode (UME) positioned at a defined (known) distance from a crystal surface. The etch pits formed at various etch times were measured using white light interferometry to ascertain pit dimensions. To determine quantitative dissolution kinetics, a moving boundary finite element model was formulated in which experimental time-dependent pit expansion data formed the input for simulations, from which solution and interfacial concentrations of key chemical species, and interfacial fluxes, could then be determined and visualized. This novel analysis allowed the rate constant for proton attack on calcite, and the order of the reaction with respect to the interfacial proton concentration, to be determined unambiguously. The process was found to be first order in terms of interfacial proton concentration with a rate constant k = 6.3 (± 3) x10^{-4} m s^{-1}. Significantly, this value is similar to previous macroscopic rate measurements of calcite dissolution which averaged over large areas and many dislocation sites, and where such sites provided a continuous source of steps for dissolution. Since the local measurements reported herein are

mainly made in regions without dislocations, this study demonstrates that dislocations and steps that arise from such sites are not needed for fast proton-promoted calcite dissolution. Other sites, such as point defects, which are naturally abundant in calcite, are likely to be key reaction sites.

Introduction

The dissolution and precipitation of calcite has been investigated for more than a century.[1] Among many areas of interest, calcite dissolution is pertinent to understanding the global cycling of minerals,[2] the weathering of carbonate rocks,[3] the regulation of the earth's aquatic environments,[4] the scaling corrosion of pipes[5] and the neutralization of acidic lakes,[1] which is a major global problem.[6]

The rate and mechanism of calcite dissolution are strongly pH-dependent,[7] with the rate increasing dramatically with decreasing pH and being dominated by the direct attack of protons for pH < 4.[5] Indeed, measuring the intrinsic dissolution kinetics at pH < 4 has proved to be extremely challenging. Until 1990,[1] the proton-promoted reaction was considered to be transport-controlled based on studies with powders[7b,8] in suspension and of single crystals (generally cleaved ($10\bar{1}4$) Iceland Spar)[1,7b,9] in a rotating disk (RD) format.[7b,9a,9b,10] The introduction of the channel flow method with electrochemical detection (CFMED)[1,9c-g] allowed measurements at single crystal surfaces with greatly improved control of mass transport. Thus, using the CFMED, the heterogeneous kinetics of proton attack on calcite was elucidated for the first time,[1,9c,9d] as a consequence of the high mass transport rates that could be generated, such that surface kinetics could be observed. The surface process was found to be governed by first-order kinetics in the interfacial concentration of protons, with a heterogeneous rate constant of 4.3 (± 1.5) x 10^{-4} m s^{-1}.[5,9d] This value was corroborated later with direct *in-situ* atomic force microscopy (AFM) measurements of the dissolution process, using a specially designed flow cell, from which a heterogeneous rate constant of 3.5 x 10^{-4} m s^{-1} was deduced for the first-order heterogeneous process.[11]

The CFMED studies, and other investigations, have demonstrated that the proton-promoted dissolution of the calcite ($10\bar{1}4$) surface involves the formation and expansion of characteristic etch pits at specific surface sites corresponding to dislocations emergent at the crystal surface. The average rates measured correspond to this pitting behavior,[1,9d,9e,9g,12] evidently representing contributions from the nucleation of steps at dislocations and the migration of those steps across the surface. The pitting process was visualized *in-situ* using a combined scanning electrochemical microscopy (SECM)-AFM[12a] format to control the proton flux (and generation time) at the calcite surface. It was demonstrated that, at low fluxes, calcite dissolved via the formation of nanoscale pits, with a typical depth of one unit cell, most likely at point defects, whereas at higher fluxes macroscopic pits dominated with an outline that mirrored the rhombohedral calcite structure, and matched long time free etching studies.[12b,13]

Given the evident formation of etch pits at dislocations in the proton-promoted dissolution of calcite, a question that arises is how important are such sites for dissolution to proceed? The issue of the role of major defects (e.g. screw dislocations) on calcite dissolution has been addressed, to some extent, by measuring the overall dissolution rate after deliberately inducing defects.[12b,12c] However, because the measurements were macroscopic, rates were averaged over all surface sites. These studies demonstrated that increased quantities of gross defects could increase the rate of dissolution, but the effect was actually rather weak. Additionally, in the proton-promoted dissolution regime no effect of different dislocation density was determined, because the rate was controlled by the slow proton diffusion rates inherent to the studies.

In this study we use scanning electrochemistry microscopy (SECM) to investigate localized proton-promoted dissolution on a length scale much smaller than the characteristic spacing between dislocations emergent on the calcite surface, so that dissolution is highly likely to be induced in surface regions far from dislocations. This provides a unique opportunity to measure dissolution kinetics without any interference of such dislocations and, by comparing the rate to macroscopic values, we are able to assess the relative importance of dislocations in the dissolution process.

This work builds on previous studies which have demonstrated SECM to be powerful for local etching studies of a wide variety of different materials.[14] In this context, the ability of SECM to target microscopic regions where the dislocation spacing was much larger than the UME size, so that a dislocation-free area could be studied,[14m] was particularly valuable for studies on $CuSO_4.5H_2O$ dissolution, which demonstrated that dislocations were very important for dissolution to proceed at low to moderate undersaturations. A further significant feature of SECM is that it is capable of promoting high mass transport (diffusion) rates[14m-r] which is of particular importance for the present studies, since proton-induced calcite dissolution is rapid and it appears simply to be controlled by diffusion to many conventional techniques, so that surface kinetic information cannot be obtained (*vide supra*). Further attributes of SECM for dissolution (etching) experiments[14] are that multiple measurements can be made on one sample, providing a relatively quick method for studying dissolution processes.

The basic experimental protocol used herein was outlined recently,[15] and is summarized briefly. An UME is employed to generate well-defined (quantitative) proton fluxes electrochemically, above a region of a calcite surface of interest. The dimensions of the resulting pit are then analyzed to deduce interfacial kinetics. An

important aspect of the present study is that experimental data are used to parameterize a finite element model for the etching process, from which interfacial fluxes and concentrations are deduced directly. This approach is powerful as *no assumptions are made about the rate law or mechanism of dissolution*. Rather, the numerical model provides local fluxes and concentration distributions directly from experimental data, from which unambiguous kinetic deductions about surface kinetics can be made. This approach should be widely applicable to SECM etching studies, and to a variety of localized etching investigations.

Experimental

Materials and Solutions

All experiments were performed in 0.1 M potassium nitrate (KNO_3) (Sigma-Aldrich, purity ≥ 99.995 %) made up in Milli-Q reagent grade water. Naturally occurring single crystals of Iceland Spar (Richard Tayler Minerals, UK) were cleaved along the $(10\bar{1}4)$ cleavage plane, using an open Stanley blade (Stanley Tools USA, no. 1992) to produce two freshly exposed faces. One face was used for proton-promoted etching via SECM, while the other 'mirror' face was free-etched in 0.1 M KNO_3 at pH 6 for 60 min, to reveal sub-surface dislocations emerging at the crystal surface.[12c] Comparison of the two mirror faces after both types of etching allowed correlation of the local SECM measurements with the corresponding surface properties (*vide infra*).

Instrumentation and Procedures

The instrumentation used for SECM measurements was recently described in full.[15] Briefly, UMEs used as tips for SECM were produced in-house by sealing ≈ 1 cm length of 25 μm diameter platinum wire in a glass capillary and polishing to give a

well-defined disk-in-disk geometry with the ratio of glass to wire diameter at the probe end (RG) equal to 10.[16] The quasi-reference electrode was a 5 cm length of Ag wire coated in AgCl, while the UME acted as the working electrode in a standard two-electrode voltammetric-galvanostatic set-up.

Positioning of the tip at a precise distance from the surface was achieved using two different techniques: (i) approach curves for diffusion-limited oxygen reduction (hindered diffusion response);[15,17] and (ii) intermittent contact (IC)-SECM.[18] For IC-SECM, the tip was mounted directly onto a piezo bender actuator (PICMA P-871.112, Physik Instrumente) with a strain guage sensor (SGS) operating with an amplifier/servo (E-651.1S, Physik Instrumente). A sine wave generator (Digimess TG100, Digimess) was used to generate a sinusoidal oscillation of $\delta\sin(2\pi ft)$ in the position of the tip normal to the surface, about the average height of the tip. In an approach curve for IC-SECM, the tip was approached normal to the surface, having set the oscillation in the bulk ca. δ = 90 nm. IC was determined to be the point at which the oscillation amplitude dropped by 5 %, detected by the bender actuator; see Figure 1 for a typical IC-SECM approach curve. The tip was then withdrawn by the distance of 10 µm from the substrate, such it that was sufficiently close for the electrochemical process at the tip to promote dissolution, but also allowed dissolution products to escape; rather than accumulate significantly in the gap between the tip and the surface which might influence the etching process (e.g. by promoting back reactions).[15]

A current of 100 nA (204 A m^{-2}) was typically employed to induce the dissolution process, by oxidizing water to produce protons, which is a quantitative reaction that allows the precise calculation the proton flux at the electrode surface. [19] The duration of etching was varied accurately between 1 and 5 minutes. It is

important to note that varying the time for dissolution serves to vary the distance between the tip and (dissolving) surface, and hence the mass transport rate, allowing its influence to be determined (*vide infra*). By moving the tip to a new location after each etch, by ≈ 200 μm, numerous etches could be made on one sample. There was naturally some free etching on the SECM-etched surface (at the bulk pH = 6), but this was negligible compared to the SECM-induced proton-promoted dissolution (*vide infra*). After a series of etches was complete, the calcite sample was rinsed for ≈ 5 seconds in Milli-Q reagent grade water and mounted on a glass slide. This did not cause further significant dissolution, but produced a clear surface for visualization.

Etch Pit Visualization

The calcite 'matched faces' (SECM-etched and free-etched) were imaged by optical microscopy, typically at ×200 magnification in DIC (differential interference contrast) mode. SECM etch pits were analyzed using white light interferometry (WLI) (WYKO NT-2000 Surface Profiler, WYKO Systems) which required sputter-coating the calcite surfaces with gold (Sputter Coater, Quorum Technologies) to give a layer of ≈ 10 nm. The gold coating thickness was negligible compared with the pit depths (*vide infra*). WLI yielded 3D images of localized dissolution pits, from which various parameters were extracted for input into the numerical model for dissolution kinetics (*vide infra*).

Theoretical Analysis and Simulations

Numerical simulations were performed on a Dell Intel Core 2 Duo 2.53 GHz computer equipped with 8 GB of RAM and running Windows XP Professional 64 Bit 2002 edition. Modeling was performed using the commercial finite element modeling package Comsol Multiphysics 3.5a (Comsol AB, Sweden), using the Matlab interface (Release 2009a) (MathWorks Inc., Cambridge, UK).

The proton-promoted dissolution reaction involves the following major processes:[1]

$$CaCO_{3(aq)} + H^{+}_{(aq)} \rightleftharpoons Ca^{2+}_{(aq)} + HCO^{-}_{3(aq)} \quad (1)$$

$$HCO^{-}_{3(aq)} + H^{+}_{(aq)} \rightleftharpoons H_2CO_{3(aq)} \rightarrow CO_{2(aq)} + H_2O_{(l)} \quad (2)$$

The time-dependent mass transport and reactions of species in solution are governed by:

$$\frac{\partial C_i}{\partial t} = D_i \nabla^2 C_i + r_i \quad (3)$$

where D_i is the diffusion coefficient of species *i*, and C_i is the concentration of species *i*. There is also ion pair formation, so that *i* can be Ca^{2+}, HCO_3^-, H^+, $CaHCO_3^+$, $CaOH^+$or H_2CO_3. ∇ is the gradient operator in axisymmetric cylindrical coordinates. r_i is the net generation of species, *i*, primarily from equilibration reactions as described by activity corrected[20] mass action rate equations. For these processes, the rate constants were taken to be so fast, so as to always be at equilibrium, with respect to equation 2. The dehydration of H_2CO_3 to CO_2 is an irreversible reaction with a rate constant of 20 s^{-1}, under the conditions of our experiments.[1] The most important species in determining the etching behavior is H^+ and the diffusion coefficient is known with high precision.[1,21] A value of 7.6 x10^{-9} m^2 s^{-1} was appropriate for the experimental conditions. Other diffusion coefficients and pK values were obtained from reference 22. The following equilibrium constants were used (before activity correction): pK_w = 14, pK of $CaHCO_3^+$ = 1.00, pK of $CaOH^+$ = 1.29, and pK of H_2CO_3 = 3.76. We also used $D_{Ca^{2+}}$ = 7.92 x10^{-10} m^2 s^{-1}, together with $D_{HCO_3^-}$ = $D_{H_2CO_3}$ = $D_{CaHCO_3^+}$ = 1.2 x10^{-9} m^2 s^{-1}, which is reasonable given the similar size of these entities and the low charge density on the ions.

The axisymmetric cylindrical domain for the solution of equation 3 is shown in Figure 2. The shape of the domain was dynamic to allow for changes in the substrate topography, induced by the etching process, and was updated during the simulation of dissolution (*vide infra*).

There is a no-flux condition normal to all boundaries for each species, *i*, unless otherwise stated; i.e.:

$$\nabla C_i \cdot \underline{n} = 0 \qquad (4)$$

where $\underline{n}$ is the inward unit vector normal to the surface.

On boundary **3**, the galvanostatic generation of protons is described by: [19]

$$D_{H^+} \frac{\partial C_{H^+}}{\partial z} = i_{app} \Big/ \left(\pi F a^2 \right) \qquad (5)$$

where i_{app} is the applied current (taken to be positive in sign), F = 96485 C mol^{-1} is the Faraday constant, and a is the electrode radius. For boundaries **6** and **7**:

$$C_{H^+} = 10^{-\,pH_{init}} \Big/ \gamma_{H^+} \qquad (6)$$

where pH_{init} is the initial (bulk) solution pH and γ_{H^+} is the activity coefficient for protons (which has a value of 0.776 for the conditions herein[1]). For all other species, the following holds on boundaries **6** and **7**:

$$C_i = 0 \qquad (7)$$

The flux on boundaries **8** and **9** is due to the dissolution process described in equation 1. In contrast to our recent work,[15] an innovation for the present studies was to use experimental data for the change in the pit shape with time, as an input for the model to determine the surface kinetics directly. The flux of protons into the calcite surface causes a release of Ca^{2+} and HCO_3^- according to:

$$D_{H^+} \nabla C_{H^+} \cdot \underline{n} = - \, v_N r \qquad (8)$$

$$D_{Ca^{2+}} \nabla C_{Ca^{2+}} \cdot \underline{n} = v_N r \quad (9)$$

$$D_{HCO_3^-} \nabla C_{HCO_3^-} \cdot \underline{n} = v_N r \quad (10)$$

where v_N is the velocity in the direction normal to the surface (inward taken as positive) and r is the molar density of calcite, which is 2.706 x 10^4 mol m^{-3}.[22]

Movement of the boundaries was described as follows: boundaries **3**, **4**, **5** and **6** were fixed, while boundaries **1** and **7** were fixed in *R* but free to move in *Z* and movement of boundary **2** was fixed in *z*, but allowed to vary in *r*. The movement of boundaries **8** and **9** was determined from experimental measurements of pit depth and volume as a function of time. The shape of the pit was approximated as a truncated cone, as this shape provided a reasonably good description of a typical pit (Figure 3), from the assessment of a body of data.

Briefly, a fixed mesh was defined for the initial geometry. As the dissolution reaction proceeded, pit growth occurred and the simulation domain adapted to reflect the new geometry. Distortions to the domain were implemented through an arbitrary Lagrange-Eulerian (ALE) method. The following partial differential equation, whose variables are the coordinates in the deformed geometry, was solved:

$$\frac{\partial^2 f}{\partial x^2} + \frac{\partial^2 f}{\partial y^2} + \frac{\partial^2 f}{\partial y^2} = 0 \quad (11)$$

Equation 3 was thus solved in this coordinate frame, avoiding costly re-meshing procedures. Further details of the ALE method may be found elsewhere.[23]

Results and Discussion

Figure 4 shows a typical example of two cleaved and etched matched surfaces of a calcite crystal: (a) is the SECM-etched surface showing 2 dominant SECM pits (100 nA for 300 s) along with background pits and (b) is the corresponding free-

etched surface on which small pits (4-8 μm^2 and surface coverage $\approx 10^4$ cm^{-2}) are formed. These background pits coincide on the 2 images and mark screw and edge dislocations,[1,12d,19,24] emergent at the calcite surface. Also evident on both images are very small pits in the background which are formed at point defects.[1,12a,12d,19,24] It is evident that the amount of free etching is negligible compared to the proton-promoted dissolution in (a). Evidently, Figure 4 shows that most SECM measurements will, in fact, be made in regions free from the influence of screw and edge dislocations, presenting a clear opportunity to study dissolution in dislocation-free areas, i.e. to elucidate dissolution only in areas with point defects.

Figure 5 illustrates the effect of etch time, showing a typical WLI micrograph (a) and the corresponding pit cross sections (b), after etching times of 120, 180, 240 and 300 seconds. It is evident that the pit depth is linear with time over this range and the proton-promoted SECM-induced pits are the only significant features on the surface. This provides evidence for considering SECM-induced dissolution as the main process on an otherwise relatively inert surface.

For analysis using the model outlined, experimental SECM pit data were analyzed to deduce the change in pit depth and volume as a function of time. The data were split randomly into 3 sets, each comprising 6 repeat etches at each time (times of 60 s, 120 s, 180 s, 240 s and 300 s), such that 90 pits were analyzed overall. Figure 6 summarizes typical data from a set, showing that both etch pit depth and volume are a linear function of time; the error bars report two standard deviations of 6 repeats at each etch time.

The slopes of these plots, for each set, were used to parameterize the dissolution models. As highlighted above, the SECM-pits were well described as truncated cones.

For this pit geometry, the time-dependent radius of the pit bottom was deduced directly from:

$$r_1(t) = \frac{1}{2}\left(\sqrt{\frac{4V(t)}{\pi \cdot d(t)} - \frac{\theta(t)^2 \cdot d(t)^2}{3}} - \theta(t) \cdot d(t) \right) \quad (12)$$

where $r_1(t)$ is the radius at the bottom of the pit, $\theta(t)$ is the slope of the pit wall (dr/dz), $d(t)$ the depth, and $V(t)$ is the volume. The first term in eq 12, $V(t)/\pi\, d(t)$ is the dominant term, whereas the angle of the pit wall (within the range measured) was not as significant. With a knowledge of $r_1(t)$, the radius at the top of the pit, $r_2(t)$, is then easily deduced:

$$r_2(t) = r_1(t) + d(t) \times \theta(t) \quad (13)$$

The parameterization of data in this way yielded quantitative information on the expansion pits as a function of time, for input into the model, and from which time-dependent concentration profiles of any of the chemical species could be deduced directly, as we illustrate next.

A typical plot of the concentration of protons at a time of 180 s, deduced from the model, is shown in Figure 7 (a). This particular zoom snapshot is a segment of the axisymmetric cylindrical SECM geometry (refer to Figure 2) focusing on the region of the gap between the tip and substrate where the pit is formed (directly under the electrode). It is evident that the region of the crystal towards the cylindrical axis of symmetry (r = 0) experiences the highest mass transport, because this is directly under the center of the UME (shortest diffusion path between the tip and surface). Thus, flux and concentration data in this portion of the pit provide the optimal configuration for observing the interfacial kinetics with the highest precision (*vide infra*). Furthermore, experimental data in this portion of the pit are largely free from any approximations concerning the pit geometry (good though these approximations

are; see Figure 3). For the particular case shown, it is evident that the proton concentration at the crystal/solution interface can attain values as high as 0.4 mM, a clear illustration that the process is not transport-controlled (for which $[H^+] \rightarrow 0$ would be observed).

Ultimately, we were most interested in the proton flux and concentration at the crystal/solution interface as this leads directly to kinetic information. Figure 7 (b) shows a typical plot of the normal diffusive flux and interfacial proton concentration across the crystal/solution interface in the radial direction from the axis of symmetry over a distance of 2 tip radii, for an etch time of 60 s. At the shortest time studied (least amount of etching) this correspond to the highest mass transport rate and so reveals kinetics with the highest precision. It is evident that the interfacial proton concentration is again finite and decreases with increasing radius. This highlights the point made above, that increasing *r* corresponds to a situation of a longer diffusion path between the tip and surface (more mass transport control). Correspondingly, the normal diffusive proton flux at the calcite/solution interface also decreases with the radial direction.

Importantly, the concentration and flux profile data can be combined to determine the order of the reaction with respect to the interfacial proton concentration near the crystal, $[H^+]_c$, and the dissolution rate constant, *k*. Based on earlier macroscopic experiments,[1,11] we considered a first-order process in proton concentration and derived the heterogeneous rate constant simply by applying $j = k[H^+]_c$, for the radial coordinate along the bottom of the pit. It is evident that for most of the pit radius, *k* remains essentially constant. This is excellent confirmation of the validity of first-order heterogeneous kinetics. The analysis is less accurate at larger radial distances because the proton concentration approaches zero and also because of

the approximation of the pit geometry at this location (which necessarily occur close to the pit wall). Thus, errors in the analysis of the proton concentration and flux are more prevalent.

Based on the radial concentration profile and flux analysis summarized in Figure 7, time–dependent proton-promoted dissolution kinetics were deduced by analyzing the normal proton flux, interfacial proton concentration and kinetic constant values from outputs of the simulations averaged over $r < 5$ μm. Figure 8 shows these variables plotted as function of time, derived for the 3 sets of data (a), (b), (c), while (d) is the average outcome of the 3 sets analyzed, where the error bars are 2 standard deviations. It can be seen that the kinetic profiles are highly consistent between each of the 3 sets of data, and that, in each case, dissolution is described by a reasonably consistent kinetic constant for the duration of the dissolution experiments. These individual plots, and the summary plots, reveal the following important information:

(a) The interfacial proton concentration and proton flux decreases with increasing time (pit depth) because the effective tip/substrate distance increases with time, resulting in greater diffusive (mass transport) control of the reaction. Nonetheless, the proton concentration remains at finite (significant) values, in a narrow range, with pH < 4 during the etching process, which means the surface speciation[25] is essentially constant and the surface kinetics can be measured with the model outlined.

(b) The value of k remains essentially constant with time, despite the varying surface concentration, again confirming the validity of the rate law which is first-order in interfacial proton concentration, for effective mass transport rates (interfacial fluxes) which change by at least a factor of 2 in each case.

(c) The average *k* values derived from all of the areas studied is 6.3 (± 1.3) x 10^{-4} m s^{-1}, which is similar to previous macroscopic values.[1,11] Since SECM primarily targets dislocation-free areas of the surface (*vide supra*), the analysis thus highlights that screw and edge dislocations are relatively unimportant in determining the overall kinetics of proton attack on the calcite ($10\bar{1}4$) surface under the usual conditions of proton-promoted dissolution (pH < 4). This can be rationalized because the calcite cleavage surface is also characterized by an abundance of highly reactive point defects which provide sites for dissolution.[12a] The studies herein complement earlier SECM-AFM topographical studies[12a] by providing a value for the kinetics of proton-attack in these locations.

Conclusions

This paper has described a novel approach for the quantitative study of localized proton-promoted dissolution kinetics of calcite. SECM allows multiple measurements to be performed on a sample, and the high spatial resolution of the technique (tip size << inter-dislocation spacing) means many measurements are made in surface regions that are free from screw and edge dislocations.

Data analysis has used a novel approach in which a finite element moving boundary model was parameterized directly using experimental data for the shape and dimensions of etch pits as a function of time. This model has allowed visualization and characterization of key parameters, such as the concentration and diffusive flux of the major species (exemplified through the proton maps presented herein), enabling prospective rate laws to be assessed. Confidence in the assignment of interfacial kinetics comes from the fact that the etching process continuously changes the tip/substrate separation, and hence mass transport rate/surface concentration in an

experiment, yet an essentially time-independent rate constant resulted from the analysis of data.

There continues to be significant interest in the use the SECM for localized etching[14a-l,26] and the analysis presented herein should be of general applicability. The methodology provides a means of extracting kinetics directly from etch pit geometry as function of time, without needing to specify a rate law for the etching process.

Acknowledgements

We thank the European Research Council (ERC-2009-AdG247143-QUANTIF) for support (PRU, MMM and MP) and the EPSRC for: studentship funding for C-AM under the CTA scheme (GSK co-sponsors); for a MOAC/DTC studentship for MAE; a CASE award for LAB (Unilever co-sponsor) and a project studentship (EP/H023909/1) for RAL. Some equipment used in this research was obtained through Advantage West Midlands (AWM) and part funded by the European Regional Development Fund (ERDF) in conjunction with Birmingham Science City: Innovative Uses for Advanced Materials in the Modern World (West Midlands Centre for Advanced Materials Project 2). We thank Prof. Julie Macpherson for helpful discussions and advice.

Bibliography

(1) Compton, R. G.; Unwin, P. R. *Phil. Trans. R. Soc. A* **1990**, *330*, 1-45.
(2) (a) Teng, H. H. *Geochim. Cosmochim. Acta* **2004**, *68*, 253-262; (b) Teng, H. H.; Chen, Y.; Pauli, E. *J. Am. Chem. Soc.* **2006**, *128*, 14482-14484.
(3) Finneran, D. W.; Morse, J. W. *Chem. Geol.* **2009**, *268*, 137-146.
(4) De Giudici, G. *Am. Mineral.* **2002**, *87*, 1279-1285.
(5) Dolgaleva, I.; Gorichev, I.; Izotov, A.; Stepanov, V. *Theor. Found. Chem. Eng.* **2005**, *39*, 614-621.
(6) (a) Berner, R. A.; Morse, J. W. *Am. J. Sci.* **1974**, *274*, 108-134; (b) Sverdrup, H. *Chemica Scripta* **1983**, *22*, 12-18.
(7) (a) Arvidson, R. S.; Ertan, I. E.; Amonette, J. E.; Luttge, A. *Geochim. Cosmochim. Acta* **2003**, *67*, 1623-1634; (b) Sjoberg, E. L.; Rickard, D. T. *Geochim. Cosmochim. Acta* **1984**, *48*, 485-493; (c) Sjoberg, E. L.; Rickard, D. T. *Chem. Geol.* **1984**, *42*, 119-136.
(8) (a) Plummer, L. N.; Wigley, T. M. L. *Geochim. Cosmochim. Acta* **1976**, *40*, 191-202; (b) Chou, L.; Garrels, R. M.; Wollast, R. *Chem. Geol.* **1989**, *78*, 269-282.
(9) (a) Compton, R. G.; Daly, P. J.; House, W. A. *J. Colloid Interface Sci.* **1986**, *113*, 12-20; (b) Rickard, D.; Sjoberg, E. L. *Am. J. Sci.* **1983**, *283*, 815-830; (c) Compton, R. G.; Pritchard, K. L.; Unwin, P. R. *Freshwat. Biol.* **1989**, *22*, 285-288; (d) Compton, R. G.; Pritchard, K. L.; Unwin, P. R. *J. Chem. Soc., Chem. Commun.* **1989**, 249-251; (e) Compton, R. G.; Walker, C. T.; Unwin, P. R.; House, W. A. *J. Chem. Soc., Faraday Trans.* **1990**, *86*, 849-854; (f) Orton, R.; Unwin, P. R. *J. Chem. Soc., Faraday Trans.* **1993**, *89*, 3947-3954; (g) Unwin, P. R.; Barwise, A. J.; Compton, R. G. *J. Colloid Interface Sci.* **1989**, *128*, 208-222.
(10) Compton, R. G.; Daly, P. J. *J. Colloid Interface Sci.* **1984**, *101*, 159-166.
(11) Coles, B. A.; Compton, R. G.; Booth, J.; Hong, Q.; Sanders, G. H. W. *Chem. Commun.* **1997**, 619-620.
(12) (a) Jones, C. E.; Unwin, P. R.; Macpherson, J. V. *ChemPhysChem* **2003**, *4*, 139-146; (b) MacInnis, I. N.; Brantley, S. L. *Geochim. Cosmochim. Acta* **1992**, *56*, 1113-1126; (c) MacInnis, I. N.; Brantley, S. L. *Chem. Geol.* **1993**, *105*, 31-49; (d) Barwise, A. J.; Compton, R. G.; Unwin, P. R. *J. Chem. Soc., Faraday Trans.* **1990**, *86*, 137-144.
(13) Luttge, A.; Arvidson, R. S. *J. Am. Ceram. Soc.* **2010**, *93*, 3519-3530.
(14) (a) Mandler, D.; Bard, A. J. *J. Electrochem. Soc.* **1990**, *137*, 2468-2472; (b) Mandler, D.; Bard, A. J. *Langmuir* **1990**, *6*, 1489-1494; (c) Bragato, C.; Daniele, S.; Baldo, M. A.; Denuault, G. *Ann. Chim. (Rome)* **2002**, *92*, 153-161; (d) Combellas, C.; Fermigier, M.; Fuchs, A.; Kanoufi, F. *Anal. Chem.* **2005**, *77*, 7966-7975; (e) Combellas, C.; Kanoufi, F.; Mazouzi, D. *J. Electroanal. Chem.* **2006**, *589*, 243-248; (f) Cornut, R.; Hapiot, P.; Lefrou, C. *J. Electroanal. Chem.* **2009**, *633*, 221-227; (g) Hazimeh, H.; Nunige, S.; Cornut, R.; Lefrou, C.; Combellas, C.; Kanoufi, F. *Anal. Chem.* **2011**, *83*, 6106-6113; (h) Ktari, N.; Combellas, C.; Kanoufi, F. *J. Phys. Chem. C* **2011**, *115*, 17891-17897; (i) Macpherson, J. V.; Unwin, P. R. *J. Chem. Soc., Faraday Trans.* **1993**, *89*, 1883-1884; (j) Meltzer, S.; Mandler, D. *J. Chem. Soc., Faraday Trans.* **1995**, *91*, 1019-1024; (k) Sheffer, M.; Mandler, D. *J. Electrochem. Soc.* **2008**, *155*, D203-D208; (l) Valenti, G.; Bardini, L.; Bonazzi, D.; Rapino, S.; Marcaccio, M.; Paolucci, F. *J. Phys. Chem. C* **2010**, *114*, 22165-22170; (m) Macpherson, J. V.; Unwin, P. R. *J. Phys. Chem.* **1994**, *98*, 11764-11770; (n) Macpherson, J. V.; Unwin, P. R. *J. Phys. Chem.* **1995**, *99*, 3338-3351; (o) Macpherson, J. V.; Unwin, P. R. *J. Phys. Chem.* **1995**, *99*, 14824-14831; (p) Unwin,

P. R.; Macpherson, J. V. *Chem. Soc. Rev.* **1995**, *24*, 109-119; (q) Macpherson, J. V.; Unwin, P. R. *J. Phys. Chem.* **1994**, *98*, 1704-1713; (r) Amemiya, S.; Bard, A. J.; Fan, F. R. F.; Mirkin, M. V.; Unwin, P. R. *Annu. Rev. Anal. Chem.* **2008**, *1*, 95-131.
(15) McGeouch, C.-A.; Edwards, M. A.; Mbogoro, M. M.; Parkinson, C.; Unwin, P. R. *Anal. Chem.* **2010**, *82*, 9322-9328.
(16) Wipf, D. O.; Michael, A. C.; Wightman, R. M. *J. Electroanal. Chem.* **1989**, *269*, 15-25.
(17) Kwak, J.; Bard, A. J. *Anal. Chem.* **1989**, *61*, 1221-1227.
(18) (a) McKelvey, K.; Snowden, M. E.; Peruffo, M.; Unwin, P. R. *Anal. Chem.* **2011**, *83*, 6447-6454; (b) McKelvey, K.; Edwards, M. A.; Unwin, P. R. *Anal. Chem.* **2010**, *82*, 6334-6337.
(19) Rudd, N. C.; Cannan, S.; Bitziou, E.; Ciani, I.; Whitworth, A. L.; Unwin, P. R. *Anal. Chem.* **2005**, *77*, 6205-6217.
(20) Grime, J. M. A.; Edwards, M. A.; Rudd, N. C.; Unwin, P. R. *Proc. Natl. Acad. Sci.* **2008**, *105*, 14277-14282.
(21) Macpherson, J. V.; Unwin, P. R. *Anal. Chem.* **1997**, *69*, 2063-2069.
(22) *CRC handbook of chemistry and physics*; 90th Edition (Internet Version 2010) ed.; CRC Press/Taylor and Francis: Boca Raton, FL, 2010.
(23) Donea, J.; Huerta, A.; Ponthon, J.-P. H. In *Encyclopaedia of Computational Mechanics*; Stein, E., de Borst, R., Hughes, T. J. R., Eds.; John Wiley & Sons: Chichester, 2004, p 413-433.
(24) Compton, R. G.; Pritchard, K. L.; Unwin, P. R.; Grigg, G.; Silvester, P.; Lees, M.; House, W. A. *J. Chem. Soc., Faraday Trans. I* **1989**, *85*, 4335-4366.
(25) Van Cappellen, P.; Charlet, L.; Stumm, W.; Wersin, P. *Geochim. Cosmochim. Acta* **1993**, *57*, 3505-3518.
(26) (a) Holder, M. N.; Gardner, C. E.; Macpherson, J. V.; Unwin, P. R. *J. Electroanal. Chem.* **2005**, *585*, 8-18; (b) Jones, C. E.; Macpherson, J. V.; Barber, Z. H.; Somekh, R. E.; Unwin, P. R. *Electrochem. Commun.* **1999**, *1*, 55-60.

Figure Captions

Figure 1. IC-SECM curve of piezo oscillation for 12.5 µm radius Pt disk electrode oscillated at 80 Hz, δ = 94 nm, in 0.1 M KNO_3, approaching a calcite surface. Note the different length scales on the *x*-axis.

Figure 2. Schematic of the axisymmetric cylindrical geometry for SECM simulations. The numbers in bold signify the boundaries referred to in the text to define boundary conditions. Boundaries **2, 8** and **9** represent the shape of the calcite surface, due to pit formation, which changes over time, as deduced from experimental observations.

Figure 3. Typical cross-section of an experimental etch pit after 240 s etching (black line) and the characteristic truncated cone shape (red line) used for the finite element model.

Figure 4. DIC micrographs showing: (a) two SECM-induced etch pits on calcite obtained using 100 nA current for 300 s; and (b) the corresponding free-etched mirror face. Circles on the free etched mirror half correspond to the surface locations of the SECM etch pits in (a).

Figure 5. (a) WLI image of a set of SECM-induced etch pits at times of 120 s (1), 180 s (2), 240 s (3) and 300 s (4) etched at 100 nA. (b) Cross-section of etch pits taken from WLI image (black dashed line).

Figure 6. Example plots of: (a) pit depth vs. time; and (b) pit volume vs. time used for the parameterization of the finite element model.

Figure 7. (a) Axisymmetric plot from the FEM model depicting the proton concentration profile in the UME/surface gap for an etch time of 180 seconds at 100 nA. (b) Plots of normal diffusive flux (black solid line), concentration of protons at the crystal/solution interface close to crystal (red dashed line) and heterogeneous dissolution rate constant, *k* (blue dotted line), as a function of radius along the bottom of an etch pit for an etch time of 60 s. Data from simulations using experimentally derived pit parameters.

Figure 9. Plots of the normal diffusive flux (black solid line), proton concentration at the crystal/solution interface (red line) and first-order heterogeneous rate constant, *k* (blue line) against time (for the portion of the etch pit directly under the UME). The data in (a), (b) and (c) are the results of the numerical simulations for the three data sets and (d) is the average of these.

Figures

Figure 1

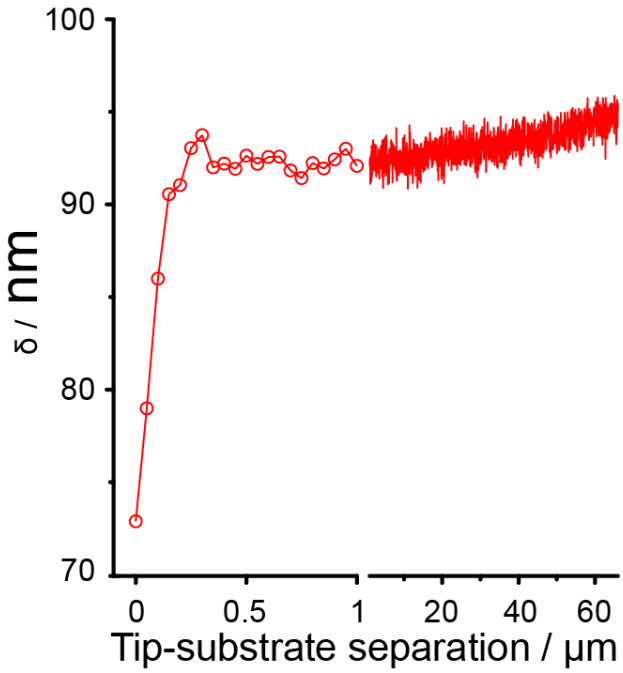

Figure 2

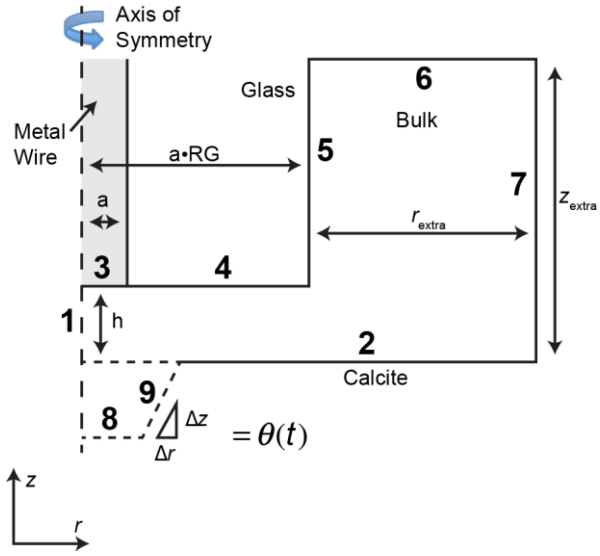
Axis of
Symmetry
Glass
6
Bulk
Metal
Wire
a•RG
5
7
z_{extra}
a
r_{extra}
3
4
1
h
2
Calcite
9
8
Δz
Δr
$= \theta(t)$
z
r

Figure 3

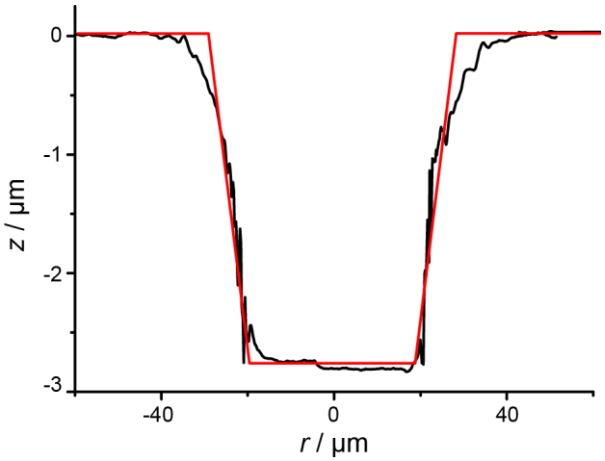

Figure 4

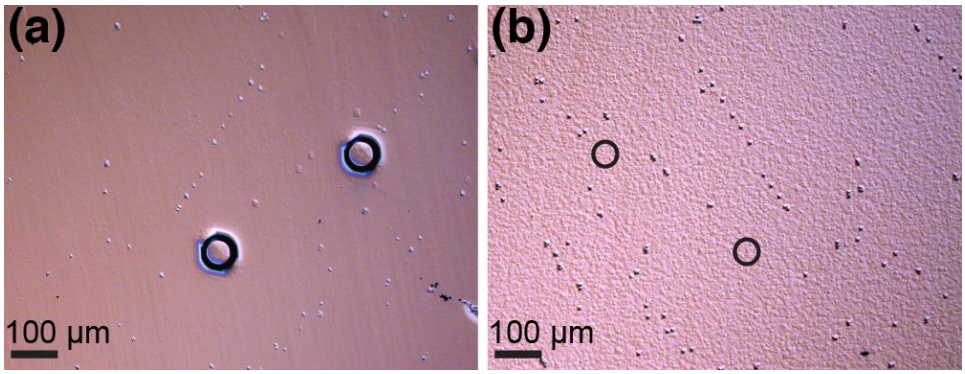

Figure 5

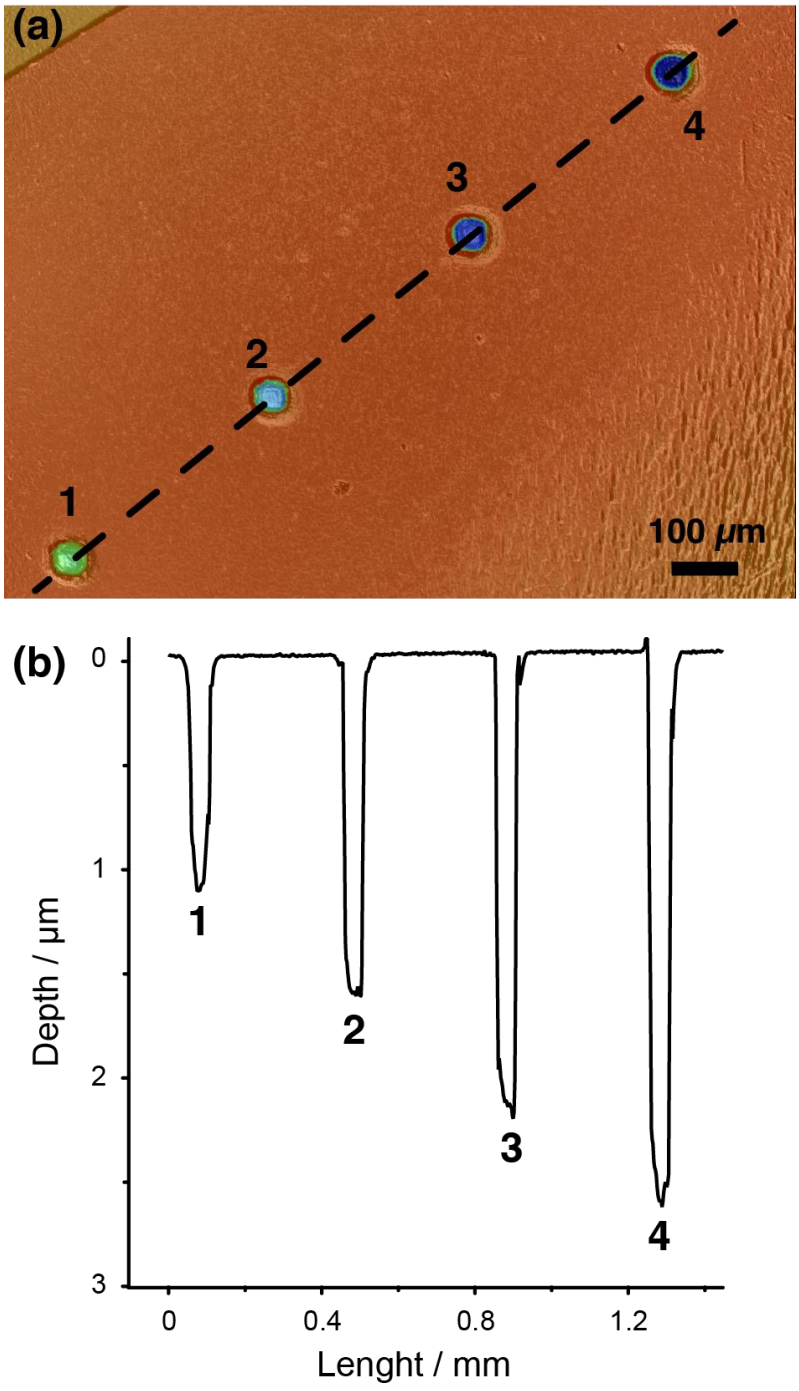

Figure 6

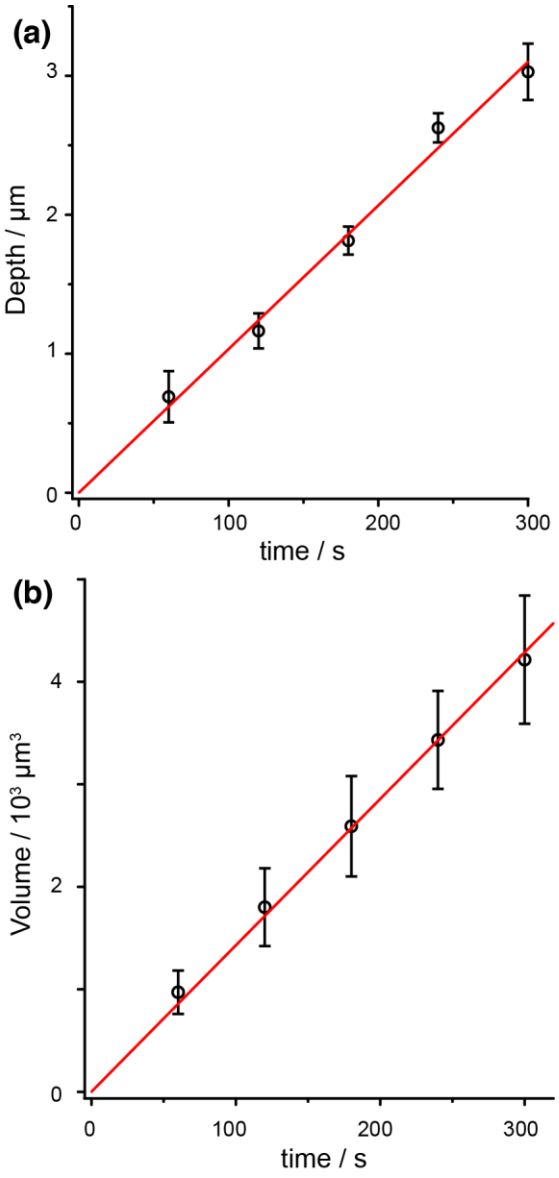
(a)
Depth / µm
0
1
2
3
0
100
200
300
time / s
(b)
Volume / 10³ µm³
0
2
4
0
100
200
300
time / s

Figure 7

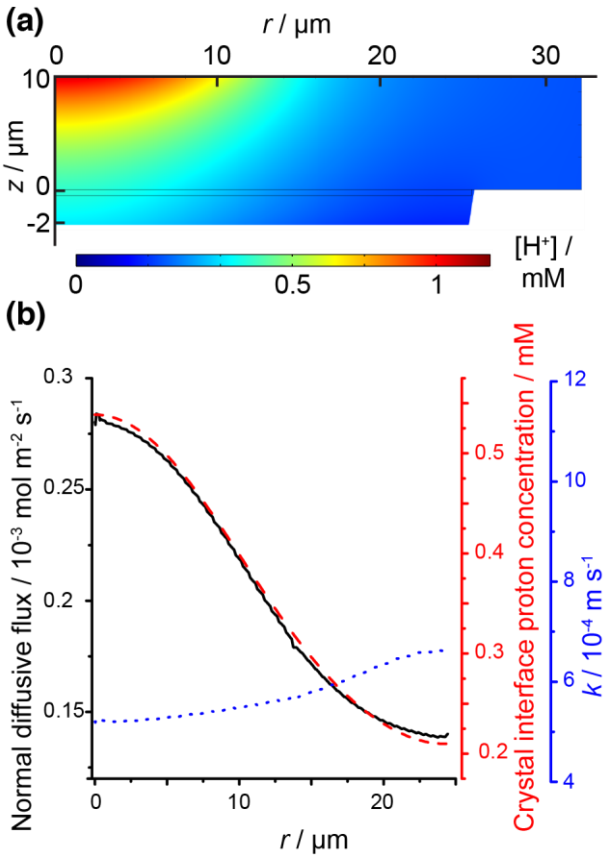
(a)
r / µm
0
10
20
30
10
z / µm
0
-2
[H+] / mM
0
0.5
1
(b)
Normal diffusive flux / 10-3 mol m-2 s-1
0.3
0.25
0.2
0.15
0
10
20
r / µm
Crystal interface proton concentration / mM
0.5
0.4
0.3
0.2
k / 10-4 m s-1
12
10
8
6
4

Figure 8

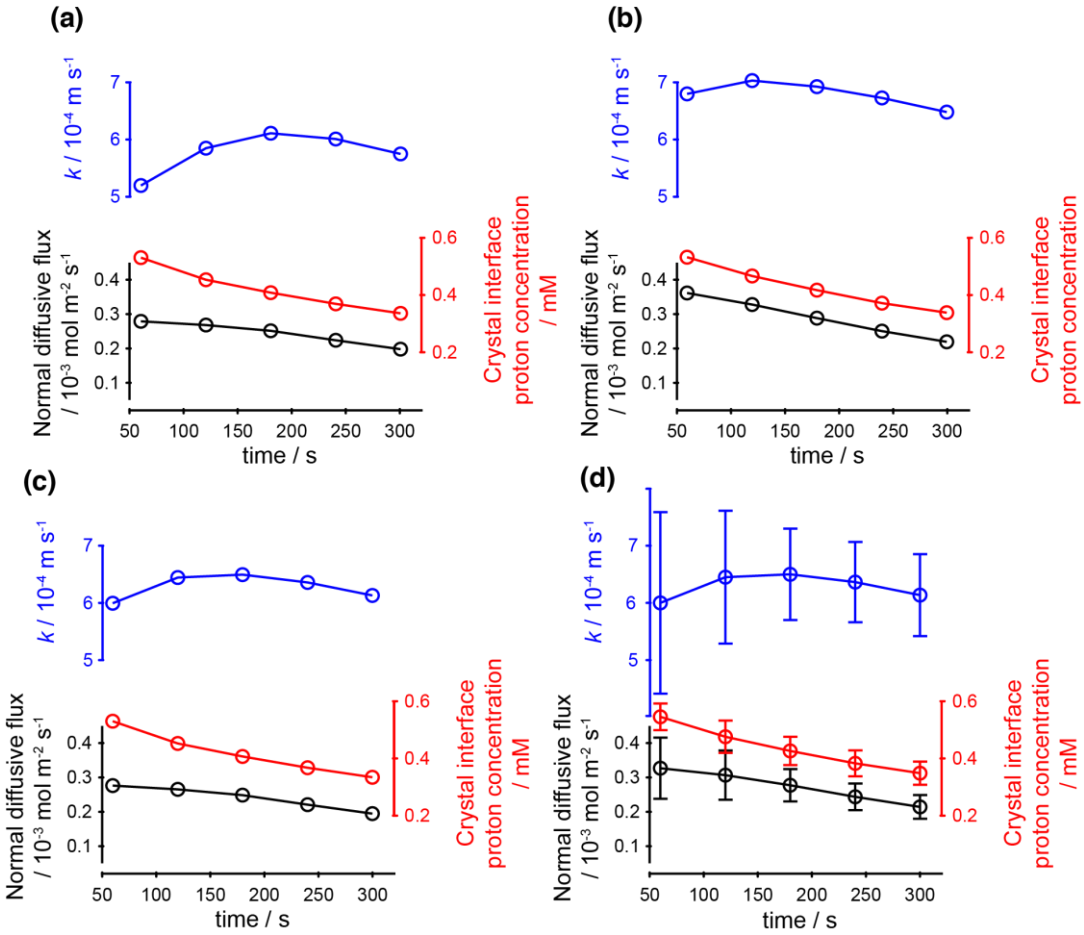
(a)
(b)
(c)
(d)
k / 10-4 m s-1
Normal diffusive flux / 10-3 mol m-2 s-1
Crystal interface proton concentration / mM
time / s

TOC